Physics of Plasmas

Numerical analysis of two-fluid tearing mode instability in a finite aspect ratio cylinder

Cite as: Phys. Plasmas **25**, 012117 (2018); https://doi.org/10.1063/1.5009389
Submitted: 16 October 2017 • Accepted: 26 December 2017 • Published Online: 22 January 2018

Atsushi Ito and Jesús J. Ramos

View Online Export Citation CrossMark

ARTICLES YOU MAY BE INTERESTED IN

Two-fluid tearing mode instability in cylindrical geometry
Physics of Plasmas **24**, 072102 (2017); https://doi.org/10.1063/1.4986116

Parameter dependence of two-fluid and finite Larmor radius effects on the Rayleigh-Taylor instability in finite beta plasmas
Physics of Plasmas **23**, 122123 (2016); https://doi.org/10.1063/1.4972819

Finite-Resistivity Instabilities of a Sheet Pinch
The Physics of Fluids **6**, 459 (1963); https://doi.org/10.1063/1.1706761

AIP Publishing

© 2018 Author(s).

Numerical analysis of two-fluid tearing mode instability in a finite aspect ratio cylinder

Atsushi Ito[1] and Jesús J. Ramos[2]
[1]*National Institute for Fusion Science, National Institutes of Natural Sciences, 322-6 Oroshi-cho, Toki 509-5292, Japan*
[2]*Plasma Science and Fusion Center, Massachusetts Institute of Technology, Cambridge, Massachusetts 02139-4307, USA*

(Received 16 October 2017; accepted 26 December 2017; published online 22 January 2018)

The two-fluid resistive tearing mode instability in a periodic plasma cylinder of finite aspect ratio is investigated numerically for parameters such that the cylindrical aspect ratio and two-fluid effects are of order unity, hence the real and imaginary parts of the mode eigenfunctions and growth rate are comparable. Considering a force-free equilibrium, numerical solutions of the complete eigenmode equations for general aspect ratios and ion skin depths are compared and found to be in very good agreement with the corresponding analytic solutions derived by means of the boundary layer theory [A. Ito and J. J. Ramos, Phys. Plasmas **24**, 072102 (2017)]. Scaling laws for the growth rate and the real frequency of the mode are derived from the analytic dispersion relation by using Taylor expansions and Padé approximations. The cylindrical finite aspect ratio effect is inferred from the scaling law for the real frequency of the mode. *Published by AIP Publishing.*
https://doi.org/10.1063/1.5009389

I. INTRODUCTION

Our previous work[1] studied the linear stability of force-free equilibria in a cylindrical geometry against two-fluid resistive tearing modes, extending the corresponding slab geometry theory for general ion skin depths[2] and carrying out a detailed benchmark between a fully numerical solution and an analytic dispersion relation derived by means of the boundary layer theory. As in the case of the slab geometry,[2–6] the two-fluid effect was found to enhance the growth rate of the cylindrical tearing mode instability compared to the single-fluid resistive magnetohydrodynamics (MHD) result.[7] The cylindrical effect on the two-fluid tearing mode was found to be stabilizing like in the single-fluid case.[7] Due to the combination of cylindrical and two-fluid effects, the mode acquires a real frequency and scaling laws for the mode growth rate and real frequency were derived from two-fluid resistive MHD neglecting finite-Larmor radius (FLR) effects for force-free equilibria. In the slab geometry, a real frequency associated with the diamagnetic drifts introduced with FLR effects would appear if the equilibrium had a pressure gradient.[8,9]

Although the analytic dispersion relation was derived for arbitrary values of the cylindrical aspect ratio, the numerical analysis of Ref. 1 examined only a case where the cylindrical effect was small. Nevertheless, the scaling laws that were derived suggested that the real frequency increased with the cylindrical effect and could become comparable to the growth rate for values of the relevant aspect ratio parameter of order unity. In addition, it was observed that the components of the inner eigenfunction solution exhibit different behaviors when their variation with respect to the cylindrical and the two-fluid parameters is considered. This paper concentrates on the case where the cylindrical effect is large and studies in more detail the dependence of eigenvalues and eigenfunctions on the finite aspect ratio cylindrical parameter.

The dispersion relation for the two-fluid resistive tearing mode instability in the cylindrical geometry shows the dependence of the mode growth rate and real frequency on the ion skin depth, through different regimes that range from the single-fluid MHD limit to the electron MHD limit. High frequency modes with immobile ions described by the electron MHD and cylinder-like structures are both observed in space plasmas as well as in laboratory plasmas. The dispersion relation that was derived from the simple two-fluid model and includes rich small scale physics could be used for verification of extended MHD simulations. The real frequency comparable to the growth rate may be large enough to be observed in simulations.

The paper is organized as follows: in Sec. II, we introduce the two-fluid resistive MHD model, the force-free equilibrium profiles in the cylindrical geometry adopted for our analysis and the linear eigenmode equations for the two-fluid tearing instability. The method used in the fully numerical solution of the complete system of linear eigenmode equations is also described. In Sec. III, the analytic dispersion relation of Ref. 1 is briefly reviewed. In Sec. IV, the numerical solutions of the eigenmode equations and the analytic dispersion relation are shown for cases where the cylindrical effect is large, and scaling laws for the growth rate and real frequency of the mode based on Taylor expansions and Padé approximations are derived. In Sec. V, the dependences of the eigenvalues and eigenfunctions on the two-fluid and cylindrical effects are further examined in the regime where the latter is not negligible but numerically small. A summary is given in Sec. VI.

II. BASIC EQUATIONS

We consider the system of resistive, cold-ion, two-fluid (Hall) MHD equations used in Ref. 1, as the simplest model

to investigate the effects of two-fluid physics and cylindrical geometry on the resistive tearing mode, neglecting FLR, electron inertia, and equilibrium pressure gradient effects

$$\frac{\partial \mathbf{B}}{\partial t} + \nabla \times \mathbf{E} = 0, \tag{1}$$

$$\mathbf{j} = \nabla \times \mathbf{B}, \tag{2}$$

$$\frac{\partial n}{\partial t} + \nabla \cdot (n\mathbf{u}) = 0, \tag{3}$$

$$\mathbf{E} = -\mathbf{u} \times \mathbf{B} + \frac{1}{en}(\mathbf{j} \times \mathbf{B} - \nabla p_e) + \eta \mathbf{j}, \tag{4}$$

$$m_i n \left[\frac{\partial \mathbf{u}}{\partial t} + (\mathbf{u} \cdot \nabla)\mathbf{u}\right] + \nabla p_e - \mathbf{j} \times \mathbf{B} = 0, \tag{5}$$

$$p_e = T_{e0} n, \tag{6}$$

where the electron temperature T_{e0} and the resistivity η are constant. This system is to be linearized about a force-free, cylindrical equilibrium with a vanishing density gradient and flow velocity: $\nabla \times \mathbf{B}_0 = 0$, $n_0 =$ constant and $\mathbf{u}_0 = 0$. Thus, the equilibrium magnetic field is

$$\mathbf{B}_0 = B_{0\theta}(r)\mathbf{e}_\theta + B_{0z}(r)\mathbf{e}_z \tag{7}$$

and the equilibrium current density is $\mathbf{j}_0 = \lambda_0 \mathbf{B}_0$, where

$$\lambda_0 = \frac{\mathbf{j}_0 \cdot \mathbf{B}_0}{B_0^2} = \frac{1}{rB_{0z}}\frac{d(rB_{0\theta})}{dr} = -\frac{1}{B_{0\theta}}\frac{dB_{0z}}{dr}. \tag{8}$$

The linear stability analysis considers normal-mode perturbations of the form

$$f(\mathbf{x}, t) - f_0(r) = f_1(r) \exp(im\theta + ik_z z + \gamma t) \tag{9}$$

with wavevector $\mathbf{k} \equiv (m/r)\mathbf{e}_\theta + k_z \mathbf{e}_z$. The parallel wavevector function that vanishes at the mode resonant surface r_s is

$$F(r) \equiv \mathbf{k} \cdot \mathbf{B}_0 = \frac{m}{r} B_{0\theta} + k_z B_{0z}. \tag{10}$$

We consider the following choice of profiles for a force-free cylindrical equilibrium:

$$B_{0\theta}(r) = (\varepsilon_B/q_0) B_c (r/a) \exp\left(-r^2/a^2\right), \tag{11}$$

$$B_{0z}(r) = B_c \left[1 - \frac{\varepsilon_B^2}{2q_0^2} + \frac{\varepsilon_B^2}{q_0^2}\left(\frac{1}{2} - \frac{r^2}{a^2}\right)\exp\left(-\frac{2r^2}{a^2}\right)\right]^{1/2}, \tag{12}$$

$$\lambda_0(r) = \frac{2\varepsilon_B}{q_0 a}\left(1 - \frac{r^2}{a^2}\right)\left[1 - \frac{\varepsilon_B^2}{2q_0^2} + \frac{\varepsilon_B^2}{q_0^2}\left(\frac{1}{2} - \frac{r^2}{a^2}\right)\exp\left(-\frac{2r^2}{a^2}\right)\right]^{-1/2}. \tag{13}$$

We normalize lengths to a, inverse lengths to a^{-1}, magnetic fields to B_c, and time to a/c_{Ac}, where $c_{Ac}^2 \equiv B_c^2/(m_i n_0)$. The normalized resistivity $\bar{\eta}$ is defined as $\bar{\eta} = \eta/(a c_{Ac})$. The thus normalized quantities are denoted by the overbars.

Linearizing Eqs. (1)–(5) and eliminating the pressure and density perturbations, we obtain the following equations:

$$(\bar{\gamma} + \bar{\eta}\bar{k}^2)\bar{B}_{1r} = i\bar{F}\bar{u}_{1r} + \bar{\eta}\left\{\left[\frac{(\bar{r}\bar{B}_{1r})'}{\bar{r}}\right]' - \frac{2im}{\bar{r}^2}\bar{B}_{1\theta}\right\} - i\bar{\gamma}\bar{d}_i\left(\frac{m}{\bar{r}}\bar{u}_{1z} - \bar{k}_z\bar{u}_{1\theta}\right), \tag{14}$$

$$\bar{\gamma}\left\{i\bar{k}^2\bar{u}_{1r} - m\left(\frac{\bar{u}_{1\theta}}{\bar{r}}\right)' - \bar{k}_z\bar{u}_{1z}' - \frac{2m}{\bar{r}^2}\bar{u}_{1\theta}\right\} = -\left\{\bar{k}^2\bar{F} + \frac{m}{\bar{r}}\left[\frac{(\bar{r}\bar{B}_{0\theta})'}{\bar{r}}\right]' + \bar{k}_z\bar{r}\left(\frac{\bar{B}_{0z}'}{\bar{r}}\right)'\right\}\bar{B}_{1r} + \bar{F}\left\{\left[\frac{(\bar{r}\bar{B}_{1r})'}{\bar{r}}\right]' - \frac{2im}{\bar{r}^2}\bar{B}_{1\theta}\right\} + \frac{2i\bar{k}_z\bar{B}_{0\theta}}{\bar{r}}\left(\frac{m}{\bar{r}}\bar{B}_{1z} - \bar{k}_z\bar{B}_{1\theta}\right), \tag{15}$$

$$\bar{\gamma}\left(\frac{m}{\bar{r}}\bar{u}_{1z} - \bar{k}_z\bar{u}_{1\theta}\right) = i\bar{F}\left(\frac{m}{\bar{r}}\bar{B}_{1z} - \bar{k}_z\bar{B}_{1\theta}\right) + \left[\frac{m}{\bar{r}}\bar{B}_{0z}' - \frac{\bar{k}_z(\bar{r}\bar{B}_{0\theta})'}{\bar{r}}\right]\bar{B}_{1r}, \tag{16}$$

$$(\bar{\gamma} + \bar{\eta}\bar{k}^2)\bar{B}_{1\theta} = i\bar{k}_z(\bar{B}_{0z}\bar{u}_{1\theta} - \bar{B}_{0\theta}\bar{u}_{1z}) - (\bar{B}_{0\theta}\bar{u}_{1r})' + \bar{\eta}\left\{\left[\frac{(\bar{r}\bar{B}_{1\theta})'}{\bar{r}}\right]' + \frac{2im}{\bar{r}^2}\bar{B}_{1r}\right\} - i\bar{\gamma}\bar{d}_i(\bar{k}_z\bar{u}_{1r} + i\bar{u}_{1z}'), \tag{17}$$

$$\left(\bar{\gamma}^2 + \bar{k}_z^2\beta\right)\bar{u}_{1z} = \frac{\bar{\gamma}\bar{B}_{0\theta}}{\bar{k}_z}\left[-\bar{k}^2\bar{B}_{1\theta} + \frac{im}{\bar{r}^2}(\bar{r}\bar{B}_{1r})'\right] - i\bar{\gamma}\bar{B}_{0z}'\bar{B}_{1r} + \frac{\bar{k}_z\beta}{\bar{r}}\left[(\bar{r}\bar{u}_{1r})' + im\bar{u}_{1\theta}\right], \tag{18}$$

where $\bar{d}_i \equiv m_i^{1/2}/(ae n_0^{1/2})$ is the ion skin depth normalized to a, $\beta \equiv T_{e0}/(m_i c_{Ac}^2)$, and

$$\bar{k}^2 \equiv \frac{m^2}{\bar{r}^2} + \bar{k}_z^2. \tag{19}$$

The prime denotes differentiation with respect to $\bar{r}$. From $\nabla \cdot \mathbf{B} = 0$,

$$\frac{(\bar{r}\bar{B}_{1r})'}{\bar{r}} + \frac{im}{\bar{r}}\bar{B}_{1\theta} + i\bar{k}_z\bar{B}_{1z} = 0. \tag{20}$$

Eliminating, further, $\bar{u}_{1\theta}$, $\bar{u}_{1z}$ and $\bar{B}_{1z}$, the normal-mode system for $(\bar{u}_{1r}, \bar{B}_{1r}, \bar{B}_{1\theta})$ is obtained.

We solve numerically the complete set of normal-mode equations on a sufficiently fine mesh that resolves the fine-scale singular layer and yields the global eigenfunctions. The eigenmode equations for $(\bar{u}_{1r}, \bar{B}_{1r}, \bar{B}_{1\theta})$ are numerically solved to obtain eigenvalues of $\bar{\gamma}$ and eigenfunctions. We calculate the radial component of the fluid displacement $\bar{\xi}$ and the non-ideal part of the z-component of the perturbed magnetic field $\bar{Q}$ to compare with the inner solutions of the boundary layer theory obtained in Ref. 1 using the relations

$$\bar{\xi} = \bar{u}_{1r}/\bar{\gamma}, \tag{21}$$

$$\bar{Q} = \frac{im^2}{\bar{k}_z\bar{k}^2\bar{r}^2}\left(\bar{B}_{1r}' + \frac{\bar{B}_{1r}}{\bar{r}}\right) - \frac{m}{\bar{r}\bar{k}_z}\bar{B}_{1\theta} + \frac{im\bar{\lambda}_0}{\bar{r}\bar{k}^2}\bar{B}_{1r}. \tag{22}$$

We consider the region $0 \le \bar{r} \le 2.0 = 2\bar{r}_s$ with a fixed boundary at $r_W = 2.0a$. The boundary conditions at $\bar{r} = 0$ and $\bar{r} = 2.0$ are

$$\bar{u}_{1r}(0) = \bar{B}_{1r}(0) = \bar{B}_{1\theta}(0) = 0, \tag{23}$$

$$\bar{u}_{1r}(2.0) = \bar{B}_{1r}(2.0) = 0, \tag{24}$$

$$\bar{Q}(2.0) = 0. \tag{25}$$

The condition (24) is the fixed boundary condition for radial perturbations. We use the condition (25) on $\bar{Q}$ only as a boundary condition at $\bar{r} = 2.0$. We discretize the variables by taking the sixth order finite differences with 100 000 intervals in the region $0 \le \bar{r} \le 2.0$ with the boundary conditions (23)–(25) to obtain a matrix equation. We find the eigenvalue of $\bar{\gamma}$ that satisfies the equation that the determinant of the matrix of the coefficients is zero. Substituting this solution of $\bar{\gamma}$, the matrix equation is solved to obtain the eigenfunctions. We choose $\beta = 0.1$ as a high beta value.

III. ANALYTIC DISPERSION RELATION

To compare with the numerical eigenvalues, the analytic dispersion relation obtained in Ref. 1 is also solved. That dispersion relation for resistive two-fluid tearing modes in a high-beta plasma cylinder was based on the boundary layer theory for singular perturbations.[6] It was obtained in the limit of small resistivity, characterized by large values of the dimensionless Lundquist number at the resonant surface, $S \equiv \bar{B}_{0s}/(\bar{\eta}\bar{k}_s) \gg 1$, where $\bar{k}_s = \bar{k}(\bar{r}_s)$ and $\bar{B}_{0s} = |\bar{\mathbf{B}}_0(\bar{r}_s)|$. The normalized growth rate $\bar{\gamma}$ is proportional to a fractional power of $\bar{\eta}$ and much less than unity. Therefore, resistive and inertial effects are only important within a narrow layer near the resonant surface $\bar{r}_s$. In our model, the only physical effect that can produce tearing instability is the resistivity. If, in our model, we set $\bar{\eta} = 0$ and keep the two-fluid terms, there is no reconnection at all because the magnetic field would be frozen into the electron fluid. To obtain high reconnection rates independent of $\bar{\eta}$ found in other simulations, other physical mechanisms for sources of reconnection such as electron inertia and for the enhancement of reconnection such as temperature gradients, anisotropies, ion FLR, and/or non-linear effects, like interactions with other instabilities and the coupling of inflow and out-flow of the diffusion region, should be included. The inner solution in a narrow layer about $\bar{r} = \bar{r}_s$, scaled as $\delta\bar{k}_s^{-1} \ll \bar{r}_s$ with $\delta \sim S^{-1/4}[\bar{\gamma}/(\bar{B}_{0s}\bar{k}_s)]^{1/4} \ll 1$, takes into account the resistive and inertial effects and will match asymptotically the ideal-MHD outer solution, regularizing its singularity and allowing for a smooth global representation of the mode. With the normalizations introduced in Sec. II, the dispersion relation is written as

$$\bar{\Delta}' = \bar{k}_s^{-1}\bar{\gamma}^{5/4}\bar{\eta}^{-3/4}|\bar{k}_s\bar{L}_B|^{1/2}\bar{B}_{0s}^{-1/2}D(\rho,\sigma), \tag{26}$$

where

$$D(\rho,\sigma) = \frac{\pi}{(1+\sigma^2/4)^{1/2}} \sum_{+,-} \left[(1+\sigma^2/4)^{1/2} \pm \sigma/2\right]^{1/2} \times \frac{\Gamma(3/4 \pm i\rho/4)}{\Gamma(1/4 \pm i\rho/4)}. \tag{27}$$

The tearing mode stability index $\bar{\Delta}'$ is calculated from the solution of the equation for $\bar{B}_{1r}$ in the outer regions outside the diffusion region written in the normalized form as

$$\left[\frac{1}{\bar{r}\bar{k}^2}(\bar{r}\bar{B}_{1r})'\right]' - \left[1 + \frac{\bar{\lambda}_0'(m\bar{B}_{0z}/\bar{r} - \bar{k}_z\bar{B}_{0\theta})}{\bar{k}^2\bar{F}} - \frac{\bar{\lambda}_0^2}{\bar{k}^2} - \frac{2m\bar{k}_z\bar{\lambda}_0}{\bar{r}^2\bar{k}^4}\right]\bar{B}_{1r} = 0, \tag{28}$$

which yield

$$\bar{\Delta}' = \frac{\bar{B}_{1r}'(\bar{r}_{s+}) - \bar{B}_{1r}'(\bar{r}_{s-})}{\bar{B}_{1r}(\bar{r}_s)}. \tag{29}$$

Two dimensionless parameters ρ and σ take, respectively, into account the effects of the cylindrical geometry and the two-fluid physics with equilibrium inverse rotational transform $q_0(r) = rB_{0z}/(RB_{0\theta})$

$$\rho = \frac{2}{|Rq_0'(r_s)|} = \frac{2\bar{k}_z^2|\bar{L}_B|}{\bar{k}_s^2\bar{r}_s}, \tag{30}$$

$$\sigma(\bar{\gamma}) = \bar{\gamma}^{1/2}\bar{\eta}^{-1/2}\bar{d}_i, \tag{31}$$

where $\bar{L}_B$ is the normalized magnetic shear length

$$\frac{1}{\bar{L}_B} = \bar{\lambda}_0(\bar{r}_s) + \frac{2m\bar{k}_z}{\bar{r}_s^2\bar{k}_s^2}. \tag{32}$$

The macroscopic lengths, $\bar{r}$, $\bar{L}_B$, $\bar{k}^{-1}$, and $\bar{\lambda}_0^{-1}$, are formally ordered as unity. Equation (30) shows that ρ is the scale length of the magnetic shear q_0' normalized to the major radius R of the periodic cylinder. In the present equilibrium with the poloidal mode number $m \sim O(1)$, ρ is finite when ε_B is finite and $\bar{r}_s \sim O(1)$ while $\rho \to 0$ when $\varepsilon_B \to 0$ or $\bar{r}_s \to \infty$. This indicates that ρ corresponds to the cylindrical effect. Equation (27) includes the special cases: $D(0, 0)$ for MHD in the slab geometry,[6] $D(0, \sigma \gg 1)$ for electron MHD in the slab geometry,[5] $D(0, \sigma)$ for two-fluid MHD with general ion skin depths in the slab geometry,[2] $D(\rho, 0)$ for MHD in the cylindrical geometry,[7] and $D(\rho, \sigma \gg 1)$ for the case in Ref. 10 in its high beta limit without the equilibrium pressure gradient though this limit was not discussed in Ref. 10. Three additional approximations were made for the boundary layer theory.[1] The first one is the "constant-ψ" approximation that neglects $(rB_{1r})' \simeq 0$ but retains $(rB_{1r})'' \neq 0$ in the inner layer equations and is valid provided $\bar{\Delta}'/\bar{k}_s = O(1)$. The second approximation is the neglect of $\bar{\eta}\bar{k}^2$ when compared to $\bar{\gamma}$, which is justified by the anticipated result that the growth rate will be proportional to a fractional (less than one) power of the resistivity. The third approximation is the restriction to a deeply subsonic regime, where $\bar{\gamma} \ll \bar{k}\beta^{1/2}$ and the fluid perturbation becomes incompressible with a growth rate independent of β. This is guaranteed for an "effectively high-β" characterized by $\beta \gg S^{-2/5}$, which is a well satisfied condition in most situations of interest.

In the present equilibrium, $\bar{\Delta}'$ is calculated from the numerical solution of the outer regions. Equation (28) is

solved numerically with a matrix solver, taking the sixth order finite differences with 100 000 intervals, subject to the boundary conditions

$$\bar{B}_{1r}(\bar{r}_s - \delta_n/2) = \bar{B}_{1r}(\bar{r}_s + \delta_n/2) \equiv \bar{B}_{1rs}, \tag{33}$$

$$\bar{B}_{1r}(0) = \bar{B}_{1r}(2.0) = 0, \tag{34}$$

where $\delta_n = 10^{-10}$. From the numerical solution for $\bar{B}_{1r}$, $\bar{\Delta}'$ is calculated as

$$\bar{\Delta}' = \frac{\bar{B}'_{1r}(\bar{r}_s + \delta_n/2) - \bar{B}'_{1r}(\bar{r}_s - \delta_n/2)}{\bar{B}_{1rs}}. \tag{35}$$

After substituting the values of $\bar{\Delta}'$ (35) and the other parameters, the dispersion relation (26) is solved numerically for $\bar{\gamma}$ by root finding methods. We choose the parameters $\bar{\eta} = 10^{-8}$, $q_0 = 0.25$, and $\bar{r}_s = 1.0$ that can be compatible with the assumption of the analytic dispersion relation $\bar{\Delta}'/\bar{k}_s = O(1)$. The normalized resistivity $\bar{\eta}$ should be small enough also for the agreement between the analytic dispersion relation and the numerical results.[1] The other parameters are also chosen to satisfy all other validity conditions for the analytic dispersion relation.

IV. RESULTS FOR ρ OF ORDER UNITY

In this section, we carry out a numerical solution of the eigenmode equations and examine the behavior of the analytic dispersion relation for a choice of parameters that yield a value of cylindrical effect parameter ρ of order unity. Taking $\varepsilon_B = 0.3$ and $m = 3$, we get $\rho = 1.033$, compared to the small $\rho = 0.09851$ used in the analysis of Ref. 1. From Secs. II and III, the other parameters result in $\bar{k}_z = -3.100$, $\bar{k}_s = 4.314$, $\bar{L}_B = -1.001$, $\bar{B}_{0s} = 0.614$, and $\bar{\Delta}' = 7.394$. The profiles of $\bar{B}_{0\theta}$, $\bar{B}_{0z}$, and $\bar{F} = \bar{\mathbf{k}} \cdot \bar{\mathbf{B}}_0$ are shown in Fig. 1. Figure 2 shows the variation of the real and imaginary parts of $\bar{\gamma}$ with the ion skin depth $\bar{d}_i$, as obtained from the fully numerical solution of the eigenmode equations and compared with the analytic dispersion relation (26). There is an excellent agreement in the range $10^{-4} \le \bar{d}_i \le 10$. The growth rate $\mathrm{Re}(\bar{\gamma})$ and the real frequency of the mode $-\mathrm{Im}(\bar{\gamma})$ are comparable with each other for $\bar{d}_i \ge 0.1$. Figure 3 shows the eigenfunctions of $\bar{B}_{1r}$ normalized to $\bar{B}_{1rs} \equiv \bar{B}_{1r}(\bar{r}_s)$ for $\bar{d}_i = 0$ and 10. The $\bar{B}_{1r}/\bar{B}_{1rs}$ eigenfunctions agree well with the outer solution Eq. (28) in the outer region. In order to further clarify the structure of the two-fluid tearing eigenfunctions and their parametric dependences on the ion skin depth, as well as the parametric dependence of the growth rate eigenvalue, we calculate the eigenfunctions $\hat{\bar{\xi}}$ and $\hat{Q}$ that determine the analytic dispersion relation (26) from the eigenfunctions $\bar{\xi}$ and $\bar{Q}$ and the eigenvalue of $\bar{\gamma}$ of the numerical solution. The two representations are related by

$$\hat{\bar{\xi}} = \frac{i\bar{\xi}^{odd}}{\bar{B}_{1rs}} (\bar{\eta}\bar{\gamma})^{1/4} \bar{B}_{0s}^{1/2} \mathrm{sign}(\bar{L}_B) \, |\bar{k}_s/\bar{L}_B|^{1/2}, \tag{36}$$

$$\hat{Q} = \frac{\bar{r}_s \bar{Q}^{odd}}{m\bar{B}_{1rs}} \bar{\eta}^{1/4} \bar{\gamma}^{-3/4} \bar{k}_s^2 \bar{d}_i \bar{B}_{0s}^{1/2} \mathrm{sign}(\bar{L}_B) \, |\bar{k}_s/\bar{L}_B|^{1/2}, \tag{37}$$

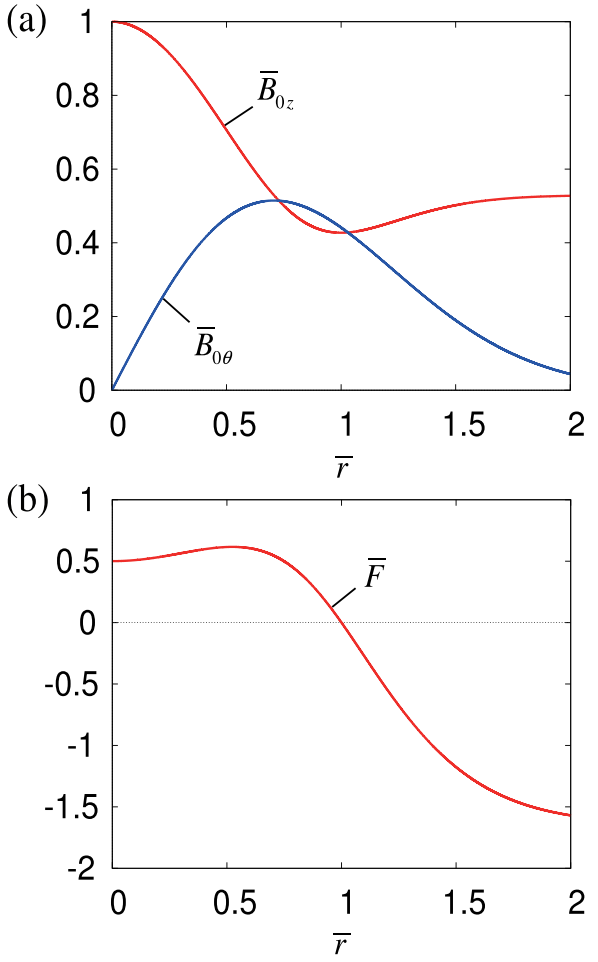

FIG. 1. Equilibrium profiles: (a) the magnetic field components $\bar{B}_{0\theta}$ and $\bar{B}_{0z}$, and (b) $\bar{F} = \bar{\mathbf{k}} \cdot \bar{\mathbf{B}}_0$ for $\varepsilon_B = 0.3$, $q_0 = 0.25$, $m = 3$, and $\bar{r}_s = 1.0$.

where $\bar{\xi}^{odd}$ and $\bar{Q}^{odd}$ are the odd parts of the eigenfunctions, extracted using

$$\bar{f}^{odd}(\bar{r}) = \frac{\bar{f}(\bar{r}) - \bar{f}(2\bar{r}_s - \bar{r})}{2}, \quad 0 \le \bar{r} \le 2\bar{r}_s, \quad \bar{f} = \bar{\xi}, \bar{Q}. \tag{38}$$

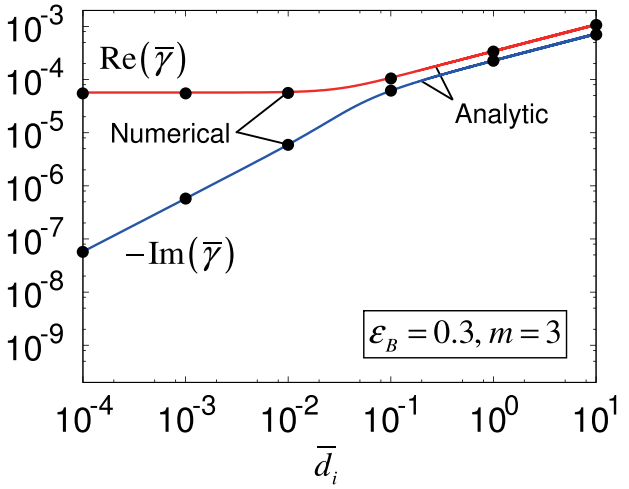

FIG. 2. Growth rates and real frequencies as functions of the ion skin depth obtained numerically from the eigenmode equations (points) compared with the analytic dispersion relation (26) (lines) for $\varepsilon_B = 0.3$ and $m = 3$.

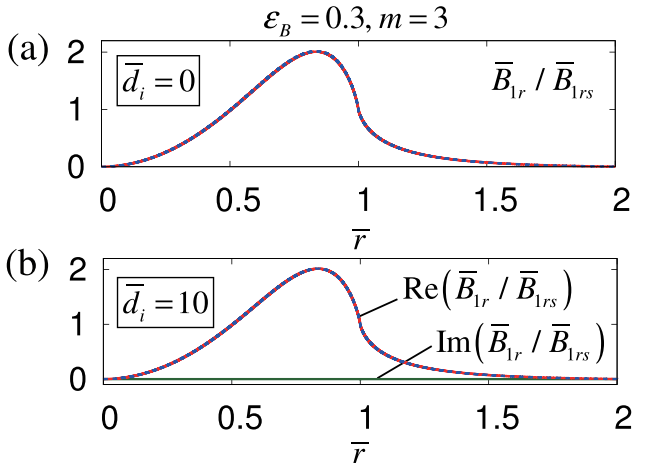

FIG. 3. Eigenfunctions of $\bar{B}_{1r}$ normalized with $\bar{B}_{1rs}$ (solid lines) compared with the numerical result for the outer solution Eq. (28) (dashed lines) for (a) $\bar{d}_i = 0$ and (b) $\bar{d}_i = 10$ for $\varepsilon_B = 0.3$ and $m = 3$.

Figures 4 and 5 show the eigenfunctions $\hat{\xi}$ and $\hat{Q}$ versus $\bar{r}$. For the single-fluid MHD case ($\bar{d}_i = 0$, Fig. 4), only the real part of $\hat{\xi}$ exists. They become complex due to the two-fluid effect (see Fig. 4 for $\bar{d}_i = 10^{-4}$ and Fig. 5 for $\bar{d}_i = 10$). In (a)–(d) of Fig. 4, $\mathrm{Re}(\hat{\xi})$ is dominant when $\bar{d}_i$ is small while, in (a)–(d) of Fig. 5, $\hat{Q}$ is dominant when $\bar{d}_i$ is large. As $\bar{d}_i$ increases, the width of $\hat{Q}$ decreases while the width of $\hat{\xi}$

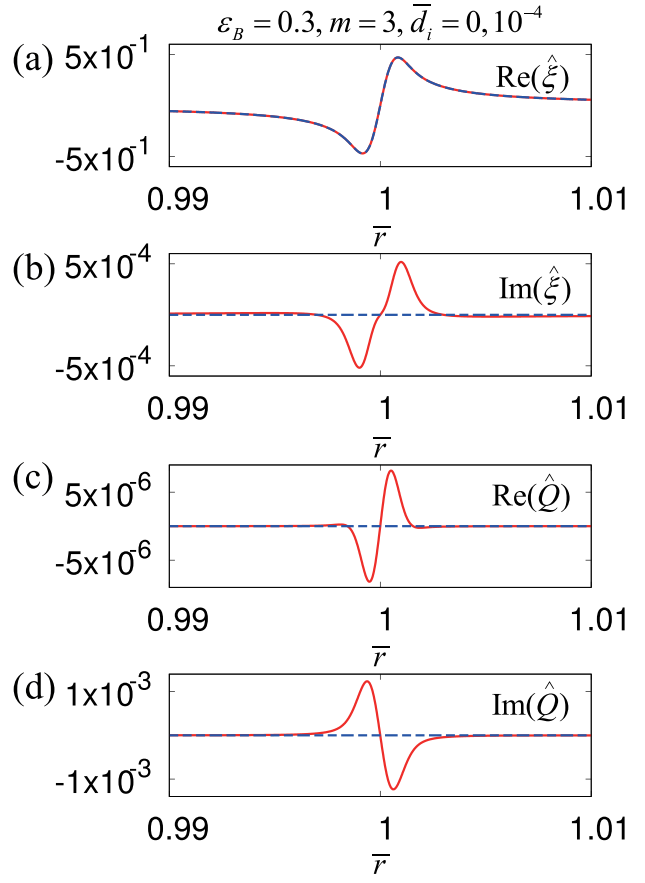

FIG. 4. Eigenfunctions of (a) $\mathrm{Re}(\hat{\xi})$, (b) $\mathrm{Im}(\hat{\xi})$, (c) $\mathrm{Re}(\hat{Q})$, and (d) $\mathrm{Im}(\hat{Q})$ for $\varepsilon_B = 0.3$, $m = 3$, and $\bar{d}_i = 0$ (dashed lines) and $\bar{d}_i = 10^{-4}$ (solid lines) obtained from the numerical eigenmodes.

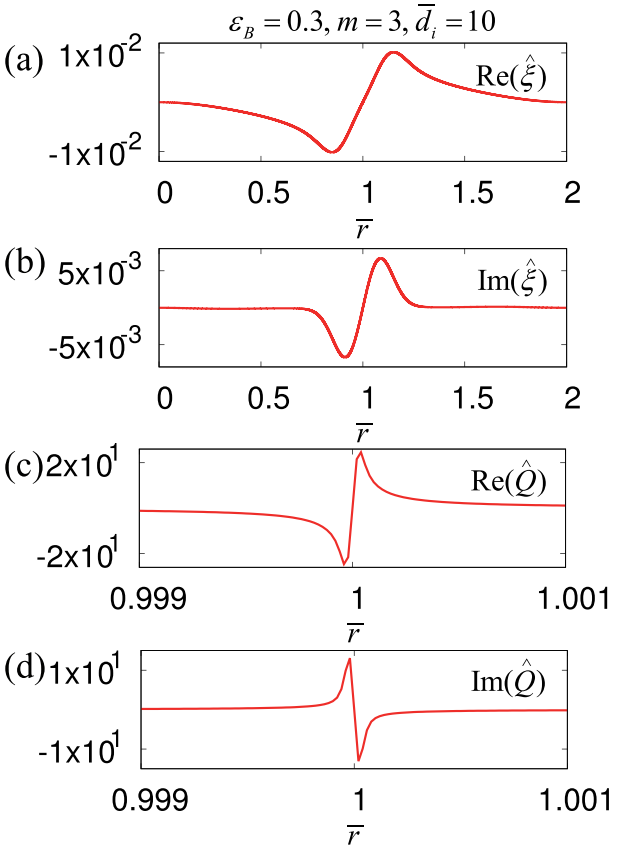

FIG. 5. Eigenfunctions of (a) $\mathrm{Re}(\hat{\xi})$, (b) $\mathrm{Im}(\hat{\xi})$, (c) $\mathrm{Re}(\hat{Q})$, and (d) $\mathrm{Im}(\hat{Q})$ for $\varepsilon_B = 0.3$, $m = 3$, and $\bar{d}_i = 10$ obtained from the numerical eigenmodes.

increases. These behaviors are the same as in the case of the small cylindrical parameter:[1] the inner solutions of the two-fluid tearing mode vary on two length scales associated with the magnetic diffusion and two-fluid effect, and the diffusion in the narrower scale enhances the growth of the tearing mode. The only difference is that, in the presently considered case where the cylindrical effect is large, the imaginary parts of the eigenfunctions are large and comparable to their real parts for finite $\bar{d}_i$. In (c) and (d) of Fig. 5, the scale length of $\hat{Q}$ for the considered $\bar{\eta} = 10^{-8}$ and $\bar{d}_i = 10$ is too narrow to be well resolved with the discrete mesh used here. Nevertheless, our sixth order finite difference gives an accurate result for the eigenvalue $\bar{\gamma}$ up to such $\bar{\eta} = 10^{-8}$ and $\bar{d}_i = 10$.

Although $\rho = 1.033$ is given by our choice of cylindrical equilibrium, we also consider the case of $\rho = 0$ (the slab limit) with the other parameters fixed in order to examine the cylindrical effect in the analytic dispersion relation (26). In the case of single-fluid MHD ($\sigma = 0$), the tearing mode is purely growing and the growth rate is $\bar{\gamma} = 5.695 \times 10^{-5}$ for $\rho = 1.033$, which shows the stabilizing effect of the cylindrical geometry compared to $\bar{\gamma} = 6.348 \times 10^{-5}$ for the slab geometry, $(\rho, \sigma) = (0, 0)$. Figure 6 shows the dependence of the real and imaginary parts of $\bar{\gamma}$ on the ion skin depth $\bar{d}_i$ for $\rho = 0$ and $\rho = 1.033$. The real part of $\bar{\gamma}$ (i.e., the growth rate) is enhanced by the two-fluid effect. The effect of the cylindrical geometry is stabilizing for each value of $\bar{d}_i$. The stabilizing effect for $\rho = 1.033$ is significant compared to the

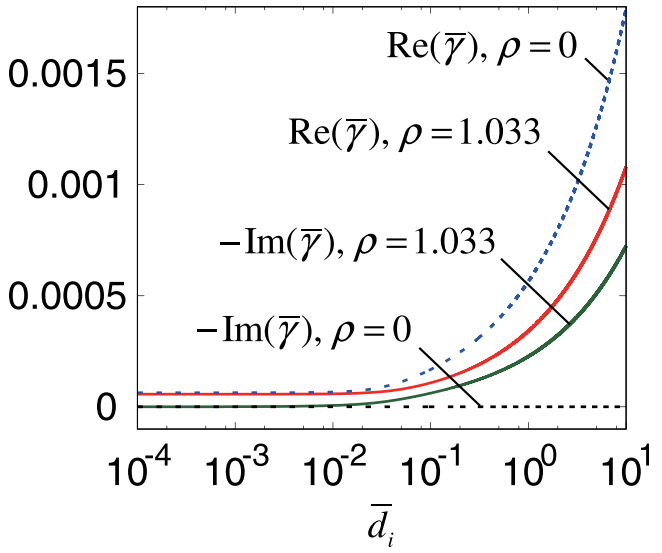

FIG. 6. Growth rates and real frequencies as functions of the ion skin depth for $m=3$ and $\rho=1.033$ (solid lines) and $\rho=0$ (dashed lines) obtained from the analytic dispersion relation (26).

small effect observed for $\rho=0.09851$ in Ref. 1. The imaginary part of $-\bar{\gamma}$ (i.e., the real frequency of the mode) arises when both the two-fluid and cylindrical effects are present and increases with $\bar{d}_i$. The growth rate and the real frequency become comparable for ρ of order unity due to the decrease of the growth rate and the increase of the real frequency.

Considering different regimes of the parameters σ and ρ, we can derive scaling laws for the growth rate and the real frequency from the analytic dispersion relation (26). For small σ and ρ, we make the Taylor expansion up to the second order

$$\bar{\Delta}' \simeq \frac{2\pi}{\bar{k}_s\bar{B}_{0s}^{1/2}}\bar{\gamma}^{5/4}\bar{\eta}^{-3/4}|\bar{k}_s\bar{L}_B|^{1/2}C_0 \times\left[\left(1+\frac{C_2}{32}\rho^2\right)\left(1-\frac{3}{32}\sigma^2\right)+\frac{iC_1}{16}\sigma\rho\right], \tag{39}$$

where

$$C_0=\frac{\Gamma(3/4)}{\Gamma(1/4)}=0.3380, \tag{40}$$

$$C_1=\frac{\Gamma'(3/4)}{\Gamma(3/4)}-\frac{\Gamma'(1/4)}{\Gamma(1/4)}=\pi, \tag{41}$$

$$C_2=-\frac{\Gamma''(3/4)}{\Gamma(3/4)}+\frac{\Gamma''(1/4)}{\Gamma(1/4)}+\frac{2\Gamma'(1/4)}{\Gamma(1/4)}C_1=4.786. \tag{42}$$

The real and imaginary parts of the dispersion relation are, respectively, given by

$$\bar{\Delta}' \simeq \frac{2\pi\bar{\gamma}_r^{5/4}}{\bar{k}_s\bar{B}_{0s}^{1/2}}\bar{\eta}^{-3/4}|\bar{k}_s\bar{L}_B|^{1/2}C_0\left\{1+\frac{C_2}{32}\rho^2-\frac{3}{32}\left(1+\frac{C_2}{32}\rho^2\right)^{-1} \times\left\{\left[1+\frac{\rho^2}{32}\left(C_2-\frac{13\pi^2}{15}\right)\right]^2+C_3\rho^4\right\}\bar{\gamma}_{r0}\bar{\eta}^{-1}\bar{d}_i^2\right\}, \tag{43}$$

$$\bar{\gamma}_i \simeq -\frac{\pi\bar{\gamma}_{r0}^{3/2}}{20}\bar{\eta}^{-1/2}\bar{d}_i\rho\left(1+\frac{C_2}{32}\rho^2\right)^{-1} =-\frac{\pi}{20}\left[\frac{\bar{k}_s\bar{B}_{0s}^{1/2}}{2\pi}C_0^{-1}\bar{\Delta}'|\bar{k}_s\bar{L}_B|^{-1/2}\left(1+\frac{C_2}{32}\rho^2\right)^{-1}\right]^{6/5} \times\bar{\eta}^{2/5}\bar{d}_i\rho\left(1+\frac{C_2}{32}\rho^2\right)^{-1}, \tag{44}$$

where $\bar{\gamma}_r=\mathrm{Re}(\bar{\gamma})$, $\bar{\gamma}_i=\mathrm{Im}(\bar{\gamma})$, and

$$\bar{\gamma}_{r0}=\left[\frac{\bar{k}_s\bar{B}_{0s}^{1/2}}{2\pi}C_0^{-1}\bar{\Delta}'|k_s\bar{L}_B|^{-1/2}\left(1+\frac{C_2}{32}\rho^2\right)^{-1}\right]^{4/5}\bar{\eta}^{3/5}, \tag{45}$$

$$C_3=\frac{13\pi^2}{7680}\left(C_2-\frac{13\pi^2}{30}\right)=0.008504. \tag{46}$$

Equation (43) shows small corrections to $\bar{\gamma}_{r0}$ due to $\bar{d}_i$. The effect of ρ in $\bar{\gamma}_{r0}$ [Eq. (45)] is stabilizing compared to the dispersion relation for MHD in the slab geometry,[6] $(\rho,\sigma)=(0,0)$, since $C_2>0$. The third term in the parentheses of the RHS of (43) shows the enhancement of the growth due to the two-fluid effect with modification due to the cylindrical effect since this term is negative for all values of ρ. Equation (44) shows that the real frequency appears due to the combination of the two-fluid and cylindrical effects and departs from the linear dependence for large ρ.

For small σ but ρ of order unity, a better result can be obtained by using a Padé approximation for the dependence on ρ while retaining the same Taylor expansion for σ. Then, the dispersion relation (26) becomes

$$\bar{\Delta}'\simeq\frac{2\pi}{\bar{k}_s\bar{B}_{0s}^{1/2}}\frac{\bar{\gamma}^{5/4}\bar{\eta}^{-3/4}|\bar{k}_s\bar{L}_B|^{1/2}C_0}{64\pi^2+C_2^2\rho^2}\left\{\left[64\pi^2+(2\pi^2+C_2)C_2\rho^2\right] \times\left(1-\frac{3}{32}\sigma^2\right)+4i\pi^3\sigma\rho\right\}. \tag{47}$$

By the definition of the Padé approximation, the Taylor expansions of Eq. (47) up to the second order in ρ coincide with Eq. (39). The real and imaginary parts of the dispersion relation are, respectively, given by the Taylor expansion of Eq. (47) up to $O(\sigma^2)$

$$\bar{\Delta}' \simeq \frac{2\pi}{\bar{k}_s\bar{B}_{0s}^{1/2}}\frac{\bar{\gamma}_r^{5/4}\bar{\eta}^{-3/4}|\bar{k}_s\bar{L}_B|^{1/2}C_0}{64\pi^2+C_2^2\rho^2}\left\{64\pi^2+(2\pi^2+C_2)C_2\rho^2 +\left\{\frac{104}{5}\frac{\rho^2\pi^6}{64\pi^2+(2\pi^2+C_2)C_2\rho^2} -\frac{3}{32}\left[64\pi^2+(2\pi^2+C_2)C_2\rho^2\right]\right\}\bar{\gamma}_{r1}\bar{\eta}^{-1}\bar{d}_i^2\right\}, \tag{48}$$

$$\bar{\gamma}_i=-\frac{16}{5}\frac{\bar{\gamma}_{r1}^{3/2}\pi^3\bar{\eta}^{-1/2}\bar{d}_i\rho}{64\pi^2+(2\pi^2+C_2)C_2\rho^2} \simeq-\frac{16}{5}\left[\frac{\bar{k}_s\bar{B}_{0s}^{1/2}}{2\pi}C_0^{-1}\bar{\Delta}'|\bar{k}_s\bar{L}_B|^{-1/2}\frac{64\pi^2+C_2^2\rho^2}{64\pi^2+(2\pi^2+C_2)C_2\rho^2}\right]^{6/5} \times\frac{\pi^3\bar{\eta}^{2/5}\bar{d}_i\rho}{64\pi^2+(2\pi^2+C_2)C_2\rho^2}, \tag{49}$$

where

$$\bar{\gamma}_{r1} = \left[\frac{\bar{k}_s \bar{B}_{0s}^{1/2}}{2\pi} C_0^{-1} \bar{\Delta}' |\bar{k}_s \bar{L}_B|^{-1/2} \frac{64\pi^2 + C_2^2\rho^2}{64\pi^2 + (2\pi^2 + C_2)C_2\rho^2}\right]^{4/5} \bar{\eta}^{3/5}. \tag{50}$$

For large σ, a Taylor expansion of the dispersion relation to the second order in ρ yields

$$\bar{\Delta}' \simeq \frac{2\pi}{\bar{k}_s \bar{B}_{0s}^{1/2}} \bar{\gamma} \bar{\eta}^{-1/2} \bar{d}_i^{-1/2} |\bar{k}_s \bar{L}_B|^{1/2} C_0 \times \left(1 + \frac{i\pi}{4}\rho + \frac{C_2}{32}\rho^2\right). \tag{51}$$

The growth rate is then given by

$$\bar{\gamma}_r = \frac{\bar{k}_s \bar{B}_{0s}^{1/2}}{2\pi C_0} \bar{\Delta}' \bar{\eta}^{1/2} \bar{d}_i^{1/2} |\bar{k}_s \bar{L}_B|^{-1/2} \times \frac{1 + \frac{C_2}{32}\rho^2}{\left(1 + \frac{C_2}{32}\rho^2\right)^2 + \frac{\pi^2}{16}\rho^2}. \tag{52}$$

This shows the correction due to the cylindrical effect, which is also stabilizing compared to the dispersion relation for electron MHD in the slab geometry ($\rho = 0$ and $\sigma \gg 1$).[5] The real frequency is given by

$$\bar{\gamma}_i = -\frac{\bar{k}_s \bar{B}_{0s}^{1/2}}{8C_0} \bar{\Delta}' \bar{\eta}^{1/2} \bar{d}_i^{1/2} |\bar{k}_s \bar{L}_B|^{-1/2} \times \frac{\rho}{\left(1 + \frac{C_2}{32}\rho^2\right)^2 + \frac{\pi^2}{16}\rho^2}. \tag{53}$$

This shows the departure from the linear dependence for large ρ. With a Padé approximation for the dependence of the dispersion relation on ρ and $\sigma \gg 1$, we obtain

$$\bar{\Delta}' \simeq \frac{2\pi}{\bar{k}_s \bar{B}_{0s}^{1/2}} \bar{\gamma} \bar{\eta}^{-1/2} \bar{d}_i^{-1/2} |\bar{k}_s \bar{L}_B|^{1/2} C_0 \times \frac{8\pi + (2\pi^2 + C_2) i\rho}{8\pi + iC_2\rho}. \tag{54}$$

The growth rate is then given by

$$\bar{\gamma}_r = \frac{\bar{k}_s \bar{B}_{0s}^{1/2}}{2\pi} \bar{\Delta}' \bar{\eta}^{1/2} \bar{d}_i^{1/2} |\bar{k}_s \bar{L}_B|^{-1/2} C_0^{-1} \times \frac{64\pi^2 + (2\pi^2 + C_2)C_2\rho^2}{64\pi^2 + (2\pi^2 + C_2)^2\rho^2}. \tag{55}$$

The real frequency is given by

$$\bar{\gamma}_i = -\frac{8\pi^2 \bar{k}_s \bar{B}_{0s}^{1/2} \bar{\Delta}' \bar{\eta}^{1/2} \bar{d}_i^{1/2} |\bar{k}_s \bar{L}_B|^{-1/2} C_0^{-1} \rho}{64\pi^2 + (2\pi^2 + C_2)^2\rho^2}. \tag{56}$$

Figure 7 shows the dependence on the ion skin depth $\bar{d}_i$ of the real and imaginary parts of $\bar{\gamma}$, compared with the scaling laws for $\sigma \ll 1$ and $\sigma \gg 1$. In Fig. 7(a), the dotted lines for $\sigma \ll 1$ and $\sigma \gg 1$ are obtained from the Taylor expansions of the dispersion relation (43) and (52), respectively, and the dashed lines for $\sigma \ll 1$ and $\sigma \gg 1$ are obtained from the Padé approximation of the dispersion relation (48) and (55), respectively. In Fig. 7(b), the dotted lines for $\sigma \ll 1$ and $\sigma \gg 1$

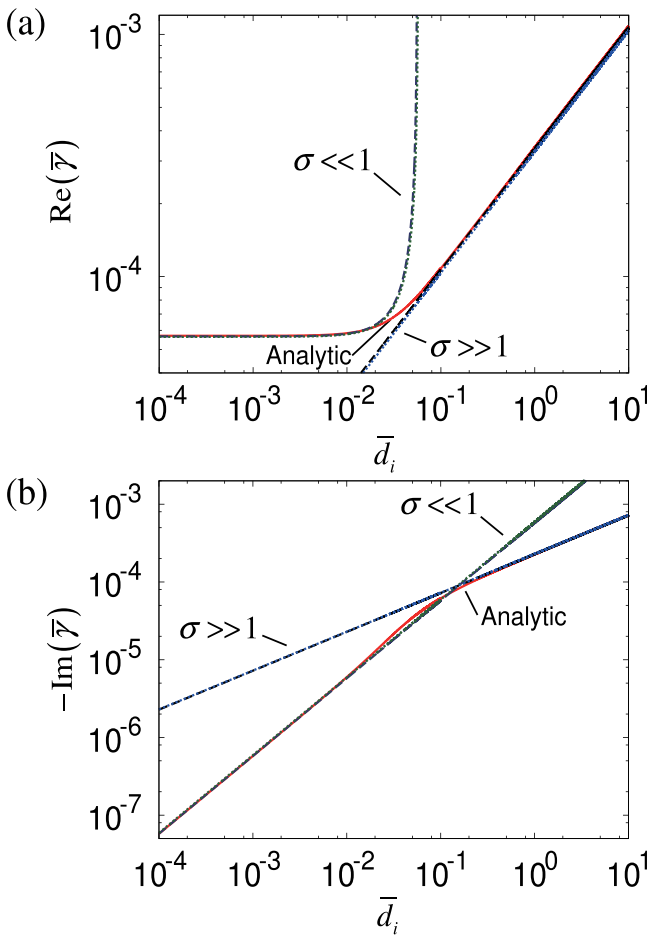

FIG. 7. (a) Growth rates and (b) real frequencies as functions of the ion skin depth for $\rho = 1.033$ and $m = 3$ obtained from the analytic dispersion relation (26) (solid lines) compared with its Taylor expansions (dotted lines) and Padé approximations (dashed lines) in ρ for $\sigma \ll 1$ and $\sigma \gg 1$.

are obtained from the Taylor expansions of the dispersion relation (44) and (53), respectively, and the dashed lines for $\sigma \ll 1$ and $\sigma \gg 1$ are obtained from the Padé approximation of the dispersion relation (49) and (56), respectively. Figure 7 shows that the dispersion relation (26) is well approximated by both the Taylor expansions and the Padé approximations for small $\bar{d}_i \leq 0.01$ and for large $\bar{d}_i \geq 1$. The differences between the Taylor expansions and the Padé approximations are small in the present results, but the accuracy for $|\bar{\gamma}|$ of the Padé approximations is slightly better than that of the Taylor expansions. The errors from the analytic dispersion relation are ∼1% for the Taylor expansion and ∼0.6% for the Padé approximation for $\bar{d}_i \ll 1$, and ∼2.6% for the Taylor expansion and ∼1% for the Padé approximation for $\bar{d}_i \gg 1$. It is noted that, since σ must be self-consistent with $\bar{\gamma}$, the resulting $\bar{\gamma}$ must satisfy the assumptions $\sigma \ll 1$ and $\sigma \gg 1$, which are satisfied for $\bar{d}_i \ll 1$ and $\bar{d}_i \gg 1$, respectively, for $\bar{\eta} \ll 1$ as shown in Fig. 7. Equations (44), (49), (53), and (56) show that the real frequency is proportional to the fractional power of resistivity as the growth rate. Hence, the real frequency appears due to the combination of resistivity, two-fluid, and cylindrical effects with zero-temperature ions and constant equilibrium electron pressure, unlike diamagnetic effects. It is mentioned

in Ref. 11 that two-fluid tearing instability becomes oscillatory due to the cylindrical effect, without explicit results to compare.

V. PARAMETRIC STUDY OF THE DEPENDENCE ON TWO-FLUID AND CYLINDRICAL EFFECTS FOR SMALL ρ

Here, we examine the dependence of the numerical eigenmodes on the two-fluid and cylindrical effects, comparing with the approximations of the analytic dispersion relation and the inner eigenfunctions derived in Ref. 1 for small ρ. Although the value of ρ can be independently set in the analytic dispersion as in Fig. 6, a parametric study of the dependence on ρ, consistent with a set of different equilibrium profiles, must be done for numerical eigenmodes. We choose two values of the parameter $\varepsilon_B = 0.05$ and 0.1 that give different values of small ρ for $q_0 = 0.25$, $\bar{r}_s = 1.0$, and $m = 2$. From Sec. III, for $\varepsilon_B = 0.05$, the other parameters result in $\rho = 0.074$, $\bar{k}_z = -0.149$, $\bar{k}_s = 2.006$, $\bar{L}_B = -6.755$, $\bar{B}_{0s} = 0.991$, and $\bar{\Delta}' = 2.961$ while for $\varepsilon_B = 0.1$, the other parameters result in $\rho = 0.154$, $\bar{k}_z = -0.308$, $\bar{k}_s = 2.024$, $\bar{L}_B = -3.317$, $\bar{B}_{0s} = 0.965$, and $\bar{\Delta}' = 3.208$.

Figure 8 shows the dependence on the ion skin depth $\bar{d}_i$ of the real and imaginary parts of $\bar{\gamma}$ for (a) $\varepsilon_B = 0.05$ and (b) $\varepsilon_B = 0.1$. Figures 2 and 8 indicate that the difference between the growth rate and the real frequency is smaller for larger ρ. In order to further illustrate the dependence of the numerical $\bar{\gamma}$ eigenvalues on the cylindrical effect for consistent equilibrium parameters, we introduce the functions ρ_1 and ρ_2

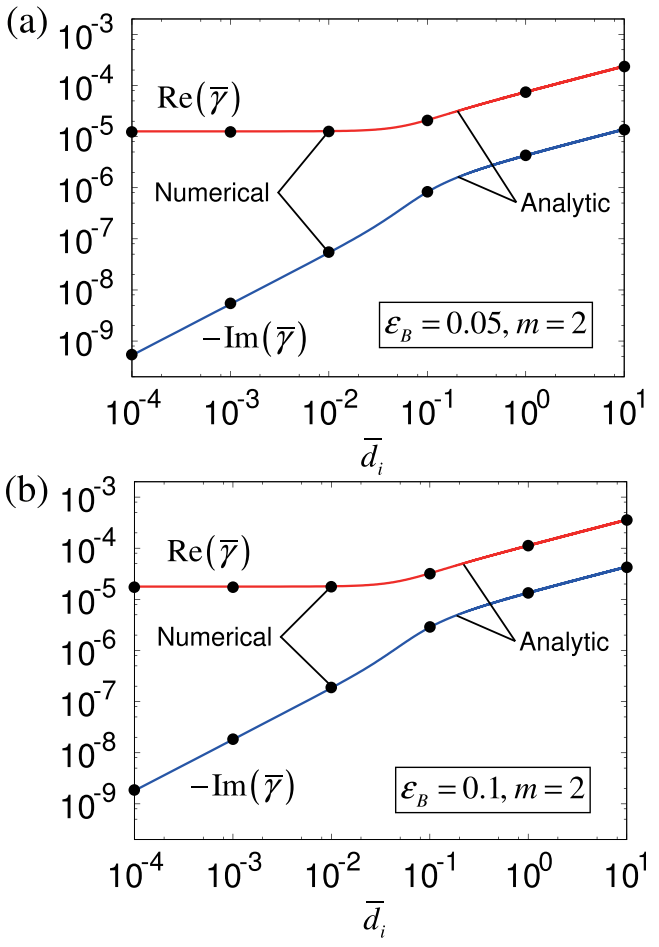

FIG. 8. Growth rates and real frequencies as functions of the ion skin depth obtained numerically from the eigenmode equations (points) compared with the analytic dispersion relation (26) (lines) for (a) $\varepsilon_B = 0.05$ and (b) $\varepsilon_B = 0.1$ for $m = 2$.

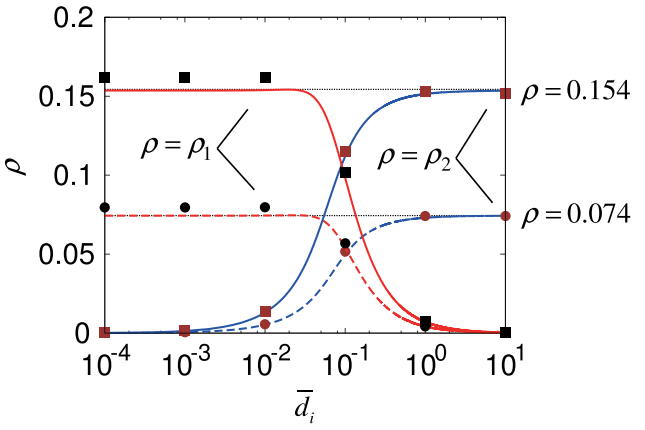

FIG. 9. The $\rho = \rho_1$ and $\rho = \rho_2$ functions, plotted against the ion skin depth for $m = 2$. The continuous curves are obtained from the analytic dispersion relation for $\varepsilon_B = 0.05$ (dashed lines) and $\varepsilon_B = 0.1$ (solid lines). The circle dots and square dots are obtained from numerical eigenvalues for $\varepsilon_B = 0.05$ and 0.1, respectively.

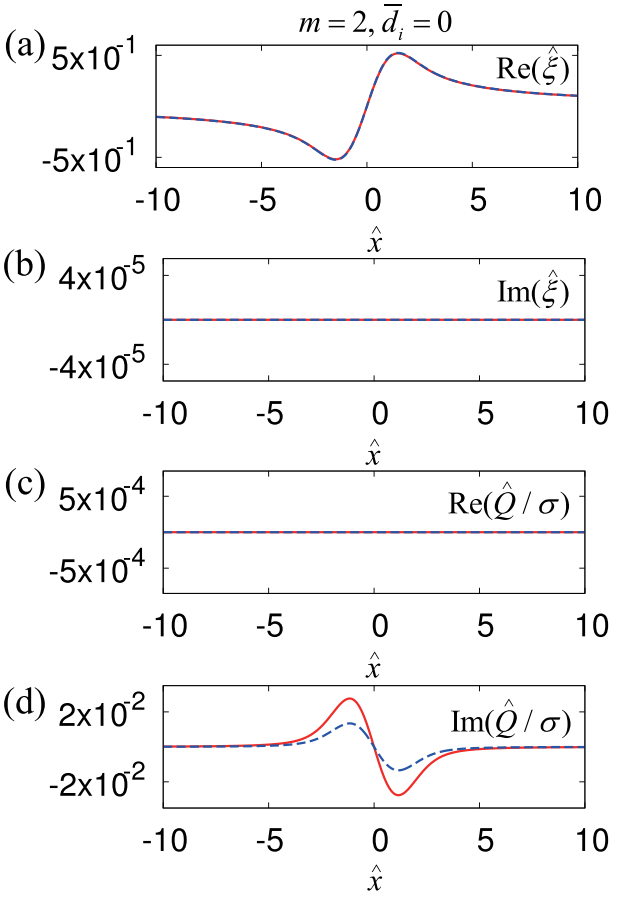

FIG. 10. Eigenfunctions of (a) Re($\hat{\xi}$), (b) Im($\hat{\xi}$), (c) Re($\hat{Q}/\sigma$), and (d) Im($\hat{Q}/\sigma$) for $\bar{d}_i = 0$, and $\varepsilon_B = 0.05$ (dashed lines) and $\varepsilon_B = 0.1$ (solid lines) obtained from the numerical eigenmodes.

defined by solving for ρ in the scaling laws for the real frequency derived in Ref. 1 for $\rho \ll 1$, respectively, in the $\sigma \ll 1$ and $\sigma \gg 1$ limits

$$\rho_1 = -\frac{20\bar{\gamma}_i \bar{\eta}^{1/2}}{\pi \bar{\gamma}_r^{3/2} \bar{d}_i} \qquad (\sigma \ll 1), \tag{57}$$

$$\rho_2 = -\frac{4\bar{\gamma}_i}{\pi \bar{\gamma}_r} \qquad (\sigma \gg 1). \tag{58}$$

Figure 9 shows the curves $\rho = \rho_1$ and $\rho = \rho_2$, where the complex growth rates obtained from the complete analytic dispersion relation and from the numerical eigenvalue solution have been substituted for $(\bar{\gamma}_r, \bar{\gamma}_i)$ in (57) and (58), for the two considered cases of $\varepsilon_B = 0.05$ and 0.1. Both in the limits of small and large $\bar{d}_i$, they show a good agreement with the physical $\rho = 0.074$ for $\varepsilon_B = 0.05$ and $\rho = 0.154$ for $\varepsilon_B = 0.1$. Thus, ρ can be estimated from the numerical eigenvalues of the growth rate and real frequency by using the scaling laws (57) and (58).

The eigenfunctions also depend on σ and ρ. Approximations of the inner solutions of $\hat{\xi}$ and $\hat{Q}$ for $\sigma \sim \rho \ll 1$ can be obtained by expanding the inner solutions with respect to σ and ρ[1] as

$$\hat{\xi} \simeq \exp\left(-\hat{x}^2/2\right) \sum_{n=0}^{\infty} \frac{2^{-2n+1/2}}{(4n+3)n!} H_{2n+1}(\hat{x}) \times \left[1 + \frac{i\rho\sigma}{4(4n+3)} O_1(\hat{x}) + \frac{\rho^2}{2(4n+3)^2} + \frac{\sigma^2}{32} O_2(\hat{x})\right], \tag{59}$$

$$\hat{Q}/\sigma \simeq \exp\left(-\hat{x}^2/2\right) \sum_{n=0}^{\infty} \frac{2^{-2n+1/2}}{(4n+3)n!} H_{2n+1}(\hat{x}) \times \left[\frac{\sigma}{4} O_1(\hat{x}) - \frac{i\rho}{4n+3}\right], \tag{60}$$

where

$$O_1(\hat{x}) = 1 + \hat{x}^2 - \frac{\hat{x}}{H_{2n+1}(\hat{x})} \frac{dH_{2n+1}}{d\hat{x}}, \tag{61}$$

$$O_2(\hat{x}) = 1 + \hat{x}^4 + \frac{\hat{x}^2}{H_{2n+1}(\hat{x})} \frac{d^2 H_{2n+1}}{d\hat{x}^2}, \tag{62}$$

$$\hat{x} = (\bar{r} - \bar{r}_s)(\bar{\eta}\bar{\gamma})^{-1/4} \bar{B}_{0s}^{1/2} |\bar{k}_s / \bar{L}_B|^{1/2}. \tag{63}$$

Figures 10–12 show the numerical solutions of the eigenfunctions $\hat{\xi}$ and $\hat{Q}/\sigma$ as functions of $\hat{x}$ for $\varepsilon_B = 0.05$ ($\rho = 0.074$) and $\varepsilon_B = 0.1$ ($\rho = 0.154$), in the cases of $\bar{d}_i = 0$ ($\sigma = 0$) and $\bar{d}_i = 10^{-4}$ ($\sigma \simeq 3.515 \times 10^{-3}$ for $\varepsilon_B = 0.05$ and σ

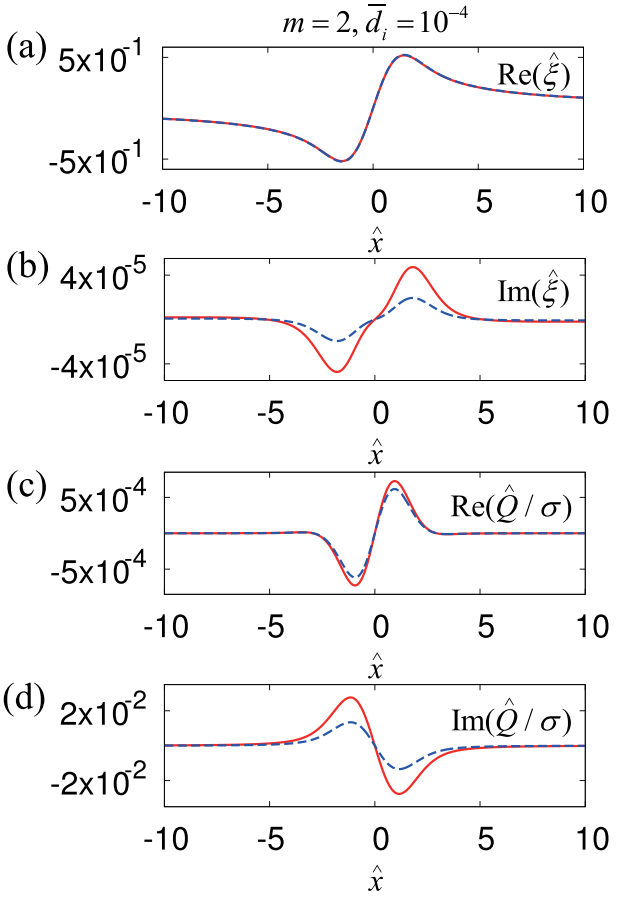

FIG. 11. Eigenfunctions of (a) $\mathrm{Re}(\hat{\xi})$, (b) $\mathrm{Im}(\hat{\xi})$, (c) $\mathrm{Re}(\hat{Q}/\sigma)$, and (d) $\mathrm{Im}(\hat{Q}/\sigma)$ for $\bar{d}_i = 10^{-4}$, and $\varepsilon_B = 0.05$ (dashed lines) and $\varepsilon_B = 0.1$ (solid lines) obtained from the numerical eigenmodes.

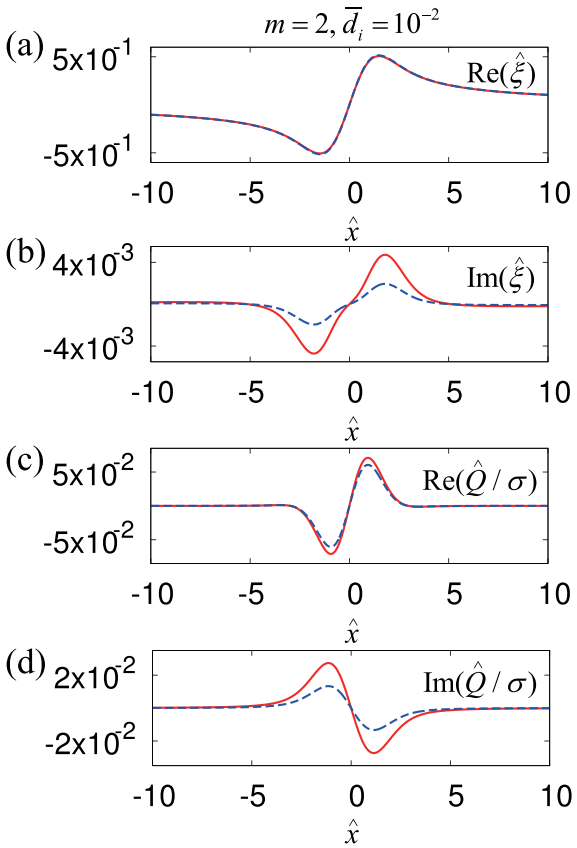

FIG. 12. Eigenfunctions of (a) $\mathrm{Re}(\hat{\xi})$, (b) $\mathrm{Im}(\hat{\xi})$, (c) $\mathrm{Re}(\hat{Q}/\sigma)$, and (d) $\mathrm{Im}(\hat{Q}/\sigma)$ for $\bar{d}_i = 10^{-2}$, and $\varepsilon_B = 0.05$ (dashed lines) and $\varepsilon_B = 0.1$ (solid lines) obtained from the numerical solution.

$\simeq 4.177 \times 10^{-3}$ for $\varepsilon_B = 0.1$) and $\bar{d}_i = 10^{-2}$ ($\sigma \simeq 3.531 \times 10^{-1}$ for $\varepsilon_B = 0.05$ and $\sigma \simeq 4.204 \times 10^{-1}$ for $\varepsilon_B = 0.1$), respectively. Equations (59) and (60) are compared with these numerical eigenfunctions. In (a) of Figs. 10–12, $\mathrm{Re}(\hat{\xi})$ is dominant and does not much depend either on ρ or $\bar{d}_i$, in agreement with Eq. (59) which tells that $\mathrm{Re}(\hat{\xi})$ is of order unity and both the cylindrical and two-fluid effects are second-order. In (b) of Figs. 10–12, $\mathrm{Im}(\hat{\xi})$ is proportional to $\rho\sigma$ and is of the order of $\rho\sigma$ compared to $\mathrm{Re}(\hat{\xi})$, in agreement with Eq. (59). In (c) of Figs. 10–12, $\mathrm{Re}(\hat{Q}/\sigma)$ is proportional to σ but does not depend on ρ, and is comparable to the first order in σ of $\mathrm{Re}(\hat{\xi})$, in agreement with Eq. (60). In (d) of Figs. 10–12, $\mathrm{Im}(\hat{Q}/\sigma)$ is proportional to ρ and does not depend on σ, and is comparable to the first order in ρ of $\mathrm{Re}(\hat{\xi})$, in agreement with Eq. (60).

VI. SUMMARY

We have studied numerically the two-fluid resistive tearing mode instability in a periodic plasma cylinder of finite aspect ratio. We have shown that when the cylindrical aspect ratio parameter is of order unity, the real frequency of the mode becomes comparable to the growth rate for finite values of the ion skin depth. This agrees very well with the boundary layer theory for singular perturbations. The imaginary parts of the eigenfunctions also become comparable with their real parts when both the cylindrical and two-fluid effects are finite. We have derived scaling laws for the growth rate and the real frequency of the mode from the finite aspect ratio analytic dispersion relation by using second order Taylor expansions and Padé approximations in the limits of small and large values of the ion skin depth. The scaling laws agree well with the analytic dispersion relation, with the Padé approximations giving a slightly better agreement. We have examined the cylindrical effect on the eigenmodes for different values of the aspect ratio of the equilibrium magnetic field. The strength of the cylindrical effect can be inferred from the numerical growth rate and real frequency eigenvalues, using the scaling law for the real frequency. The dependence of the numerical eigenfunctions on the cylindrical and two-fluid effects coincides with that of the inner solutions of the analytic boundary layer theory.

ACKNOWLEDGMENTS

This work was partially supported by the Japan/U.S. Cooperation in Fusion Research and Development, the NIFS Collaborative Research Program (Nos. NIFS17KNSS087 and NIFS16KNXN347), and by the U.S. D.O.E Grant Nos. DEFG02-91-ER54109 and DEFC02-08ER54969.

[1]A. Ito and J. J. Ramos, Phys. Plasmas **24**, 072102 (2017).
[2]E. Ahedo and J. J. Ramos, Plasmas Phys. Controlled Fusion **51**, 055018 (2009).
[3]T. Terasawa, Geophys. Res. Lett. **10**, 475, https://doi.org/10.1029/GL010i006p00475 (1983).
[4]A. B. Hassam, Phys. Fluids **27**, 2877 (1984).
[5]S. Bulanov, F. Pegoraro, and A. Sakharov, Phys. Fluids B **4**, 2499 (1992).
[6]H. P. Furth, J. Killeen, and M. N. Rosenbluth, Phys. Fluids **6**, 459 (1963).
[7]B. Coppi, J. M. Greene, and J. L. Johnson, Nucl. Fusion **6**, 101 (1966).
[8]B. Coppi, Phys. Fluids **7**, 1501 (1964).
[9]J. R. King and S. E. Kruger, Phys. Plasmas **21**, 102113 (2014).
[10]J. M. Finn and W. M. Manheimer, Phys. Fluids **26**, 962 (1983).
[11]V. V. Mirnov, C. C. Hegna, S. C. Prager, C. R. Sovinec, and H. Tian, in Proceedings of the 21st IAEA Fusion Energy Conference (2006), No. TH/P3-18.